Coupling of phase field and viscoplasticity for modelling cyclic softening and crack growth under fatigue

Coupling of Phase Field and Viscoplasticity for Modelling Cyclic Softening and Crack Growth under Fatigue

J Song[1,2], LG Zhao[2*], H Qi[1], S Li[1], D Shi[1], J Huang[1,3], Y Su[2,4] and K Zhang[2,5]

[1] *School of Energy and Power Engineering, Beihang University, Beijing 100191, China*

[2] *Wolfson School of Mechanical, Electrical and Manufacturing Engineering, Loughborough University, Epinal Way, Loughborough, LE11 3TU, UK*

[3] *School of Aeronautics and Astronautics, Central South University, Changsha Hunan 410083, China*

[4] *School of Mechanics, Civil Engineering and Architecture, Northwestern Polytechnical University, Xi'an Shaanxi, 710129, China*

[5] *School of Mechanical and Power Engineering, East China University of Science and Technology, Shanghai 200237, China.*

*Corresponding Author: L.Zhao@Lboro.ac.uk, Tel: 0044 1509 227799

Abstract

A coupled phase field-viscoplasticity approach was developed to model the deformation and crack growth in a nickel-based superalloy under fatigue. The coupled model has an advantage in predicting the cyclic softening behavior of the alloy caused by fatigue damage, overcoming a major limitation of the original cyclic viscoplasticity model. The coupled approach is also highly effective in predicting fatigue crack propagation under varied dwell times at peak load, an important behavior for crack growth under dwell fatigue. By incorporating the stress state factor, the coupled model is further utilized to investigate the growth behavior of 3D cracks

under fatigue. Both the geometrical feature of the 3D crack front and the overall crack growth rate are well captured, confirming the predicative capability of the coupled model.

Keywords: Phase field; Cyclic viscoplasticity; Cyclic softening; Fatigue crack propagation, Stress state factor.

1. Introduction

Attempt at phase field fracture modeling can be traced back to late 1990s, using a smooth function to describe the discontinuous behavior of crack initiation and propagation (Ortiz et al. 1999; Moës et al. 1999). Since then, a substantial body of work has been carried out to explore the theory and computational methods of phase field model. Generally, the phase field approach describes the sharp boundary in system as a smooth interface using a series of continuous phase field variables. In terms of fracture, the phase field approach treats the crack as a smooth transition between the fractured and intact materials. The evolution of phase field variable approximates the fracture of material as a continuous process, and can capture crack initiation, propagation, branching and merging, in good agreement with experimental results (Ambati et al. 2015). Phase field method has been further developed to study complicated crack propagation behavior in different materials, including the elastic (Miehe et al. 2014 and 2015; Hofacker et al. 2013; Singh et al. 2016;) and plastic (Miehe et al. 2015) materials. Studies have also been carried out to couple the phase field method with cyclic plasticity to simulate fatigue crack growth in metals. For instance, Haveroth (Haveroth et al. 2020) and Ulloa (Ulloa et al.

2020) proposed a strain-gradient-enhanced phase field framework, where accumulated plastic energy was used as a driving force for fatigue crack propagation. The results of numerical simulations indicated that the coupled model could describe cyclic hardening/softening and ratcheting behaviors of the material, and also objectively simulated the initiation, propagation and merging of ductile cracks.

Still, a majority of previous phase field studies focused on crack propagation in simple elastic or time-independent plastic materials, which neglected the rate-dependent inelastic deformation behavior of materials. For metals, especially at elevated temperatures, the viscoplastic behavior plays an important role in crack tip deformation and crack propagation. Firstly, viscoplasticity-induced creep behavior can influence the crack growth rate significantly. Keck et al. (1985) and Andersson et al. (2001) analyzed the stress-strain response ahead of the crack tip for viscoplastic materials. Their results showed that, under cyclic loading with dwell imposed at peak load, material deformation near the crack tip demonstrated a significant creep behavior, leading to an increase of inelastic strain near the crack tip and thus acceleration of fatigue crack propagation. Everitt et al. (2008) and Pang et al. (2016) investigated experimentally the crack growth behavior in nickel-based superalloys with different dwell periods. At elevated temperature, crack propagation rate was a function of dwell period, and the increase of dwell period would increase crack propagation rate. Secondly, viscoplastic materials possess rate-dependent mechanical behavior, which influences the stress/strain fields

near the crack tip and consequently affects crack propagation behavior. Qian et al. (1996) found that the increase of loading frequency or rate would lead to an increase of viscoplastic strain near the crack tip, thus increasing the fatigue crack propagation rate. The work of Schmidt et al. (1973) showed that the threshold of fatigue crack propagation was seen to decrease with increasing loading frequency at a given load ratio. For aluminum alloy, the threshold dropped by almost a factor of 2 when the frequency was raised from 342 to 832 Hz. Therefore, the viscoplastic behavior should be considered in modelling deformation and crack propagation, especially for metals/alloys working at elevated temperature.

In fact, numerous constitutive models have been developed to capture viscoplastic deformation of materials, especially stress-strain response and hardening/softening behaviors under cyclic load. The well-known Chaboche model employed isotropic and kinematic hardening laws to describe the cyclic hardening behavior of materials (Chaboche, 1989). However, the model can only describe the monotonic increasing of the stress range (up to a steady state after a number of cycles) and fails to describe the cyclic softening behavior. Thus, many researchers modified the constitutive model to capture both hardening and softening behaviors of materials. Ferney et al. (1994) introduced the linear softening into the kinematic hardening modulus after saturation to capture the nonlinear mechanical behaviors of alloys under both proportional and non-proportional loadings. Bernhart et al. (1999) modified the model as a two isotropic variable, depicted as a summation of an exponential and a linear decreasing term respectively, to

characterize the cyclic hardening and softening. The model corresponded well to the experimental results of steel in the temperature range of 200 °C to 500 °C. Yaguchi (2005) and Takahashi (1998) used a concept of softening surface controlled by an internal variable in the hardening rule, which was able to describe both uniaxial and multiaxial cyclic softening behaviors of 9Cr-1Mo steel. Although the viscoplastic models mentioned above were proved able to describe the cyclic softening behavior of metals/alloys under fatigue, they require more model parameters and are too complicated to use.

In addition, viscoplastic constitutive models have also been used to study crack tip deformation and crack propagation behavior in metals/alloys under fatigue. Lee et al. (2013) used viscoplatic model to characterize the crack propagation in stainless steel plate. The viscoplastic model was coupled with phase transformation and damage models to capture the strong hardening behavior caused by the strain-induced martensitic transformations near the crack tip. The simulation results agreed well with the experimental results in terms of crack propagation behavior. Kanninen et al. (1990) carried out viscoplastic dynamic simulations to study the initiation of rapid crack propagation in engineering structures and provided transferable material crack arrest toughness values in the regime where viscoplastic-dynamic conditions dominate. Recently, Zhao et al. (2008) and Tong et al. (2013) quantified the accumulation of viscoplastic strain near a crack tip and related it with material separation or fracture for several different materials, specimen geometries and loading conditions. Their results suggest that

crack propagation is mainly controlled by strain accumulation near the crack tip, independent of specimen geometries. The model was successful in predicting the crack growth under different loading waveforms (Zhao et al. 2008; Tong et al. 2002), where the fracture criterion was based on the concept of viscoplastic strain accumulation (or ratchetting strain). However, the model was essentially the original Chaboche model which did not consider the cyclic softening behavior, a major limitation of their crack growth modelling work.

In this study, a coupled phase field-viscoplasticity model was proposed, for the first time, to describe both cyclic hardening and softening behaviors of a nickel-based superalloy at elevated temperature by introducing just the fracture energy parameter. The coupled approach was further applied to study 2D crack growth in CT specimens under different model I cyclic loading conditions, focusing on the effect of dwell periods imposed at peak loads. In addition, 3D crack growth was also studied using the coupled approach, aiming to clarify the effect of varied stress state along the 3D crack front.

2. Methodology

2.1 Constitutive model for cyclic viscoplasticity

The viscoplastic constitutive relation developed by Chaboche (1989) is employed to describe the cyclic response of materials, considering both isotropic hardening (R) and kinematic hardening ($\boldsymbol{\alpha}$). According to the small-strain hypothesis, the strain rate tensor $\dot{\boldsymbol{\varepsilon}}$ is

decomposed into the elastic part $\dot{\boldsymbol{\varepsilon}}_{\mathrm{e}}$ and plastic part $\dot{\boldsymbol{\varepsilon}}_{\mathrm{p}}$,

$$\dot{\boldsymbol{\varepsilon}}=\dot{\boldsymbol{\varepsilon}}_{\mathrm{e}}+\dot{\boldsymbol{\varepsilon}}_{\mathrm{p}} \tag{1}$$

The elastic strain rate follows the Hooke's law,

$$\dot{\boldsymbol{\varepsilon}}_{\mathrm{e}}=\frac{1+\nu}{E}\dot{\boldsymbol{\sigma}}-\frac{\nu}{E}\left(tr\dot{\boldsymbol{\sigma}}\right)\mathbf{I} \tag{2}$$

where E and v represent the Yong's modulus and Poisson's ratio of the material, and $\dot{\boldsymbol{\sigma}}$ and $\mathbf{I}$ stand for the stress rate and unit tensors, respectively.

The viscoplastic strain rate tensor is expressed as

$$\dot{\boldsymbol{\varepsilon}}_{\mathrm{p}}=\left\langle\frac{f}{Z}\right\rangle^{n}\frac{\partial f}{\partial\boldsymbol{\sigma}} \tag{3}$$

where f is the function of yield surface, Z and n are the material constants. The function <•> is defined as follows,

$$\langle x\rangle=\begin{cases}x, x\geq 0\\ 0, x<0\end{cases} \tag{4}$$

The plastic flow rule is described by

$$f\left(\boldsymbol{\sigma},\boldsymbol{\alpha},R,k\right)=\sqrt{\frac{3}{2}\left(\boldsymbol{\sigma}'-\boldsymbol{\alpha}'\right):\left(\boldsymbol{\sigma}'-\boldsymbol{\alpha}'\right)}-R-k\leq 0 \tag{5}$$

where $\boldsymbol{\alpha}$ and R are the back stress and isotropic hardening variables, k is the initial radius of the yield surface, and $\boldsymbol{\sigma}'$ and $\boldsymbol{\alpha}'$ represent the deviators of stress ($\boldsymbol{\sigma}$) and back stress ($\boldsymbol{\alpha}$), respectively.

The evolution of back stress $\boldsymbol{\alpha}$ and isotropic hardening stress R obey the following rules,

$$\begin{cases} \dot{\boldsymbol{\alpha}} = \dot{\boldsymbol{\alpha}}_1 + \dot{\boldsymbol{\alpha}}_2 \\ \dot{\boldsymbol{\alpha}}_1 = C_1\left(a_1\dot{\boldsymbol{\varepsilon}}_p - \boldsymbol{\alpha}_1\dot{p}\right) \quad \text{and} \quad \dot{R} = b\left(Q - R\right)\dot{p} \\ \dot{\boldsymbol{\alpha}}_2 = C_2\left(a_2\dot{\boldsymbol{\varepsilon}}_p - \boldsymbol{\alpha}_2\dot{p}\right) \end{cases} \tag{6}$$

where C_1, C_2, a_1, a_2, b and Q are material constants, which can be determined by the cyclic stress-strain response of the material under fatigue (Zhao et al. 2001 and 2008; Nguyen et al. 2017). The accumulated plastic strain rate $\dot{p}$ is described by

$$\dot{p} = \sqrt{\frac{2}{3} d\dot{\boldsymbol{\varepsilon}}_{\mathrm{p}} : d\dot{\boldsymbol{\varepsilon}}_{\mathrm{p}}} \tag{7}$$

The multiaxial formulation of the Chaboche model has been programmed into a user-defined material subroutine (UMAT), based on the Euler backward iteration and fully implicit integration algorithms (Zhao et al. 2008). The UMAT was interfaced with ABAQUS to conduct finite element simulations in this work.

2.2 Phase field model

The phase-field simulation for damage and fracture is considered as a smeared method, in which the cracks are approximated by a serious of non-stiffness elements, capturing the discontinuities of crack-embedded materials (Nguyen et al. 2017 and 2017). Moreover, during the simulation, a continuous stiffness degradation function is adopted to capture the damage and fracture progress of materials. When the stiffness of elements reduces to zero, the elements

lose their load-bearing capacity, characterizing the discontinuities of crack initiation and propagation in the materials (i.e. full damage process).

In this study, a diffuse-interface is employed to represent the sharp crack, as shown in Fig. 1, in which Ω_h and Ω_s represent the displacement and stress boundary conditions of cracked solid Ω, respectively. Here we use a phase field function $d(x)$ to describe the initiation and propagation of cracks (Molnár et al. 2017; Fang et al. 2019; Zhang et al. 2020; Kuhn et al. 2016). The phase field function d characterizes the solids as undamaged ($d(x)$=0), damaged (0<$d(x)$<1) and fully crack ($d(x)$=1) states, given by,

$$d(x) = e^{-|x|/l_c} \tag{8}$$

where l_c represents a width scale, and x indicates the distance to crack center as shown in Fig. 2. The l_c controls the width of the crack, and has a great effect on the convergence of simulation (Bourdin et al. 2008; Schmidt et al. 2009). Here, l_c was set as 0.05 mm, covering about 8 layers of elements along the crack growth path as recommended in (Fang et al. 2019). Therefore, during the simulation, there are more than one layer of elements where the crack is expected to develop, increasing the accuracy and convergency of the simulation.

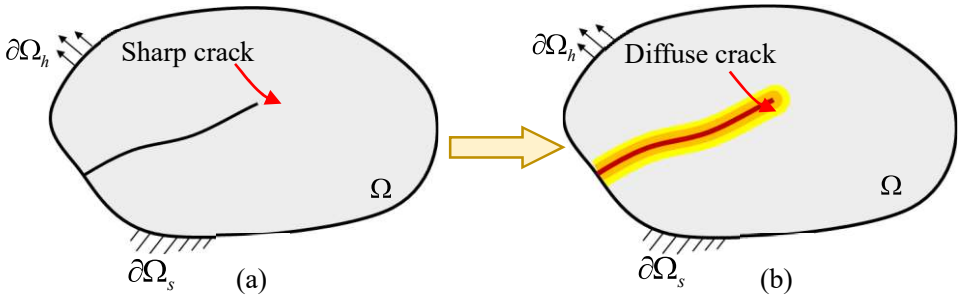

Figure 1 Schematic of the (a) sharp crack and (b) phase-field diffuse crack

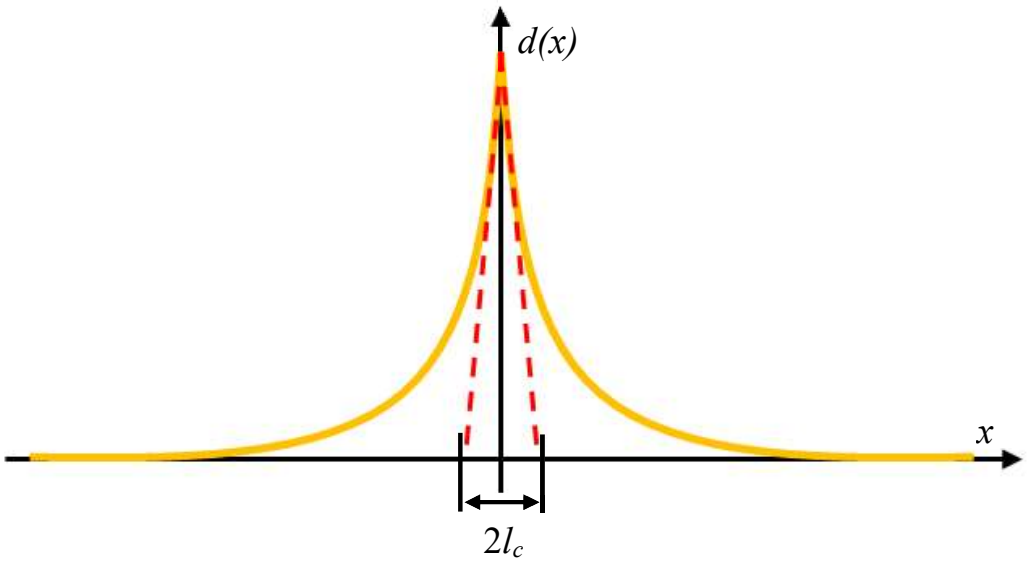

Figure 2 Phase-field diffuse crack described by Eq. (11)

During crack initiation and propagation, new surfaces are generated and consume the energy of the materials. Therefore, to establish the virtual work formulation, we need calculate the area of crack surface. Generally, the topology of cracks can be described by a diffusive representation. Then the total area of the crack surface in the cracked Ω body can be calculated by the volume integrals of the crack density function (Molnár et al. 2017; Fang et al. 2019),

$$\Gamma(d) = \int_{\Omega} \left(\frac{1}{2l_c} d^2 + \frac{l_c}{2} |\nabla d|^2 \right) \tag{9}$$

where the parameter l_c controls diffuse width of phase-field cracks (same as that in Eq. (11)). As shown in the formulation, the crack density is also related to the value of phase field d and the curl ∇d.

Then, the fracture energy of solid is approximated as,

$$\int_{\Gamma} g_f d\Gamma = \int_{\Omega} \frac{g_f}{2l_c}\left(d^2 + l_c{}^2 \nabla d \cdot \nabla d\right) d\Omega \tag{10}$$

where g_f is the fracture energy density of solid. The integral represents the total fracture energy required for crack initiation and propagation. Because the value of phase field d is assigned between 0 and 1, the maximum value of fracture energy is dependent on $g_f/2l_c$, describing the resistance to crack initiation and propagation in the materials.

2.3 Coupling phase field and cyclic viscoplasticity

Based on the framework of previous studies (Molnár et al. 2017; Fang et al. 2019; Zhang et al. 2020; Kuhn et al. 2016), here we propose an viscoplastic phase field formulation, considering the contribution of accumulated plastic strain to fatigue crack propagation (Shi et al. 1999; Jahed et al. 2006). The potential energy of a viscoplastic material consists of strain energy and crack fracture energy (Zhang et al. 2020). Therefore, the total energy in the material can be defined as,

$$\Phi = \int_{\Omega} (1-d)^2 \left(\frac{1}{2}\boldsymbol{\varepsilon}_e : \bar{\boldsymbol{\sigma}} + G_p\right) d\Omega + \int_{\Omega} \frac{g_f}{2l_c \eta}\left(d^2 + l_c{}^2 \nabla d \cdot \nabla d\right) d\Omega - \int_{\Omega} \mathbf{b} \cdot \mathbf{u} d\Omega - \int_{\partial\Omega^{\sigma}} \mathbf{t} \cdot \mathbf{u} \partial\Omega \tag{11}$$

where $\mathbf{t}$ is the external load, $\mathbf{b}$ is the body force, $\bar{\boldsymbol{\sigma}}$ represents undamaged stress tensor calculated by the viscoplastic model, G_p is the accumulated plastic strain energy, and η is the stress state factor related to the multiaxial stress state of material. On the right hand side of Eq. (11), the first term is the total strain energy of the material, and the second term represents the energy consumed by the crack initiation and propagation. The third and fourth terms are the

work done by the body force and external load, respectively.

Many studies have shown that the multiaxial stress state may have great influence on the crack and fracture behaviors (Ye et al. 2017; Chen et al. 2020; Castelluccio et al. 2016; Sajid et al. 2019). Moreover, for the propagation of 3D cracks, the stress state at different positions along the crack front might be different, which could influence the crack growth rate and change the shape of the crack front. Therefore, the critical fracture energy should be a function of the stress state (Wang et al. 2016). Here, we introduce the stress state factor η into the second term on the right side of Eq. (11), which is given as,

$$\eta=\left(\frac{3\sigma_{hyd}}{\sigma_{mises}}\right)^2 \tag{12}$$

where σ_{hyd} is the hydrostatic stress, and σ_{mises} represents the von Mises stress. A value of 1 for η represents a uniaxial stress state and has no influence on fracture energy. For plane stress, the factor is smaller compared to plane strain, therefore a higher strain energy is required for fracture, resulting in a lower crack growth rate (Algarni et al., 2019 and Bhadauria et al., 2012). In this study, it was assumed that the compressive stress state had no influence on fracture energy, and the state factor was therefore set as a value of 1. Moreover, the η was set to 1 when σ_{hyd}=0.

To capture the cyclic damage and failure of solids, we associate accumulate plastic strain energy with the total energy in Eq. (11). The rate of accumulated plastic strain energy is defined

as,

$$dG_p = d\boldsymbol{\varepsilon}_\mathbf{p} : \bar{\boldsymbol{\sigma}} \tag{13}$$

where $\boldsymbol{\varepsilon}_\mathbf{p}$ represents the plastic strain, which could be calculated by the viscoplastic constitutive model. The G_p is a nondecreasing function and corresponds to the irreversibility of phase field evolution. When the material is in elastic stage, there is no plastic strain and no plastic strain energy is accumulated (i.e. $dG_p = 0$). Therefore, G_p remains unchanged in the elastic loading and unloading stages. However, in the inelastic stage, the product of $d\varepsilon_p$ and stress $\bar{\boldsymbol{\sigma}}$ remains a positive value irrespective of tensile or compressive stress states, giving an accumulation of the plastic strain energy G_p.

The increasing value of phase field variable d represents the damage accumulated in the material. Therefore, the stress in the damaged materials decreases with the phase field variable d,

$$\boldsymbol{\sigma}(d) = \left[(1-d)^2 + \kappa \right] \bar{\boldsymbol{\sigma}} \tag{14}$$

where $\bar{\boldsymbol{\sigma}}$ is the stress without damage and computed from the viscoplastic model. When the phase field variable reaches 1, it indicates the full facture of the material and the effective stress should be reduced to zero. However, considering a zero-stiffness matrix (or effective stress) might bring a series of numerical problem, a calculation parameter κ was introduced here to avoid the problem. During the simulation, the κ is very small (10^{-6}) which has little effect on the calculation results.

For the strain energy under fatigue, the elastic part would decrease in the unloading steps due to the recovery of elastic strain. However, considering the irreversibility of crack initiation and propagation, we introduce a history function ensuring no reduction in the phase field variable during the cyclic loading (Borden et al. 2016),

$$\psi = \max\left(\frac{1}{2}\boldsymbol{\varepsilon}_e : \overline{\boldsymbol{\sigma}} + G_p\right) \tag{15}$$

where ψ is the maximum of strain energy of the loading history, and $\boldsymbol{\varepsilon}_e$ is the elastic strain.

During the calculation, when cracks initiate or propagate, the energy calculated by phase field method is equal to the fracture energy consumed by cracks, keeping the balance of energy equation as shown in Eq. (11). The solution of phase field variable d can be found iteratively by minimizing the total energy Φ (the principle of minimum potential energy), i.e., differentiating total energy with respect to the phase field variable d,

$$\frac{\partial \Phi}{\partial d} = 2\left[(1-d)+\kappa\right]\psi + \frac{g_f}{l_c\eta}\left(l_c^{\,2}\Delta d - d\right) = 0 \tag{16}$$

3. Numerical implementation within finite element framework

3.1 User defined element implementation

The viscoplastic phase field formulation is implemented by user defined element (UEL) and user defined material (UMAT) subroutines, based on the principle of minimum potential energy.

Here, the models use a two-layer structure, and the calculation results are transferred through a staggered method.

In each element, the displacement vector $\boldsymbol{u}$ and phase field variable d are defined as follows,

$$\mathbf{u} = \sum_{i=1}^{Nnode} \mathbf{N}_i^{\mathbf{u}} \mathbf{u}_i \,, \quad d = \sum_{i=1}^{Nnode} N_i^d d_i \tag{17}$$

where the $\mathbf{N}_i^{\mathbf{u}}$ and N_i^d are the shape functions, $\mathbf{u}_i$ and d_i represent the displacement vector and phase field variable at integral node, respectively. N_{node} is the number of integral nodes of each element. The strain and phase field of the element can be obtained by,

$$\boldsymbol{\varepsilon} = \sum_{i=1}^{Nnode} \mathbf{B}_i^{\mathbf{u}} \mathbf{u}_i \,, \quad \nabla d = \sum_{i=1}^{Nnode} B_i^d d_i \tag{18}$$

where $\mathbf{B}_i^{\mathbf{u}}$ and B_i^d are the derivatives of shape function.

Because of the introduction of phase field, the residual vector is composed of displacement part r^u and phase field part r^d, defined as,

$$\mathbf{r}_i^{\mathbf{u}} = \int_\Omega (1-d)^2 \left(\mathbf{B}_i^{\mathbf{u}}\right)^T \sigma d\Omega - \int_\Omega \left(\mathbf{N}_i^{\mathbf{u}}\right)^T \mathbf{b} d\Omega - \int_{\partial\Omega} \left(\mathbf{N}_i^{\mathbf{u}}\right)^T \mathbf{t} d\partial\Omega \tag{19}$$

$$r_i^d = \int_\Omega \left\{ \left[\frac{g_f}{l_c} d - 2(1-d)\psi \right] N_i + g_f l_c \left(\mathbf{B}_i^d\right)^T \nabla d \right\} d\Omega \tag{20}$$

where ψ is the accumulated strain energy calculated by the viscoplastic constitutive model using Eq. (15).

Therefore, the nonlinear equations can be solved by *Newton-Raphson* method given by,

$$\begin{Bmatrix} \mathbf{u} \\ d \end{Bmatrix}_{n+1} = \begin{Bmatrix} \mathbf{u} \\ d \end{Bmatrix}_{n} - \begin{bmatrix} \mathbf{K}^{\mathbf{u}} & 0 \\ 0 & \mathbf{K}^{d} \end{bmatrix}^{-1} \begin{Bmatrix} r^{\mathbf{u}} \\ r^{d} \end{Bmatrix}_{n} \tag{21}$$

where K^u and K^d are the displacement and phase field stiffness matrices, respectively. They are defined as,

$$\mathbf{K}_{ij}^{\mathbf{u}} = \frac{\partial \mathbf{r}_i^{\mathbf{u}}}{\partial \mathbf{u}_j} = \int_{\Omega} \left[(1-d)^2 + \kappa \right] \left(\mathbf{B}_i^{\mathbf{u}} \right)^T \mathbf{J} \mathbf{B}_j^{\mathbf{u}} d\Omega \tag{22}$$

$$\mathbf{K}_{ij}^{d} = \frac{\partial r_i^{d}}{\partial d_j} = \int_{\Omega} \left[g_f l_c \left(\mathbf{B}_i^{d} \right)^T \mathbf{B}_j^{d} + \left(\frac{g_f}{l_c} + 2\psi \right) N_i N_j \right] d\Omega \tag{23}$$

where ***J*** is the Jacobian matrix of the viscoplastic solid. Notably, the coupling effect of phase field and deformation has been considered in Eqs. (22) and (23). Thus, the mixed matrices of K^u and K^d have been set as zero in Eq. (21).

3.2 Data transfer between user elements and material nodes

Considering the crack initiation and propagation would degrade the stiffness matrix and redistribute the stress field (Miehe et al. 2010; Singh et al. 2016), the results computed at each increment should be updated and transferred between the viscoplastic and phase field subroutines. In order to pass the data between UMAT and UEL, we employ the staggered method (Molnár et al. 2017; Fang et al. 2019), where at increment *n*, the displacement field $\boldsymbol{u_n}$ is affected by the phase-field value at previous increment (d_{n-1}). Then, the value d_n is recalculated based on the new displacement field $\boldsymbol{u_n}$. The flow chart of staggered method is shown in Fig. 3. Generally, the phase field value at the *n* increment would influence the stiffness matrix and stress/strain computations at the *n+1* increment. For each increment, if the phase

field value increases too rapidly, the stiffness matrix would decrease suddenly in the next increment and the results are not properly computed between those increments. Moreover, the rapid decrease of stiffness matrix would also affect the convergency of finite element simulations. However, the effect could be improved by using small increments (Fang et al. 2019). Considering the computing efficiency and accuracy, here we set the increment as 0.001s in the finite element computations.

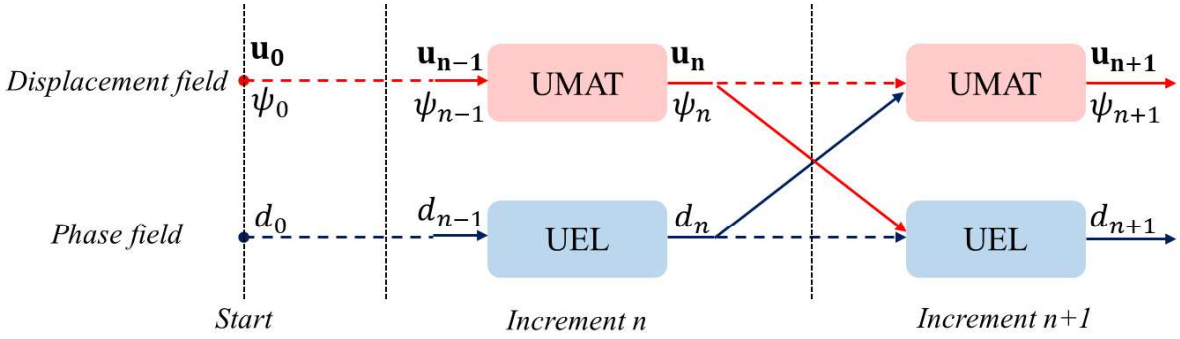

Figure 3, Flowchart of the staggered method.

To realize the data transfer, two-layer structure is employed for the finite element models in this study. Fig. 4 illustrates the two-layer structure for a 2D model. Elements in the first layer have only one phase field degree of freedom (DOF), and store the phase field value computed by the UEL subroutine; while elements in the second layer have three displacement DOF for 3D models (two DOF for 2D model), and store the displacement field, stress/strain and strain energy computed by the UMAT subroutine. Common blocks are used for data sharing between the elements of the two layers.

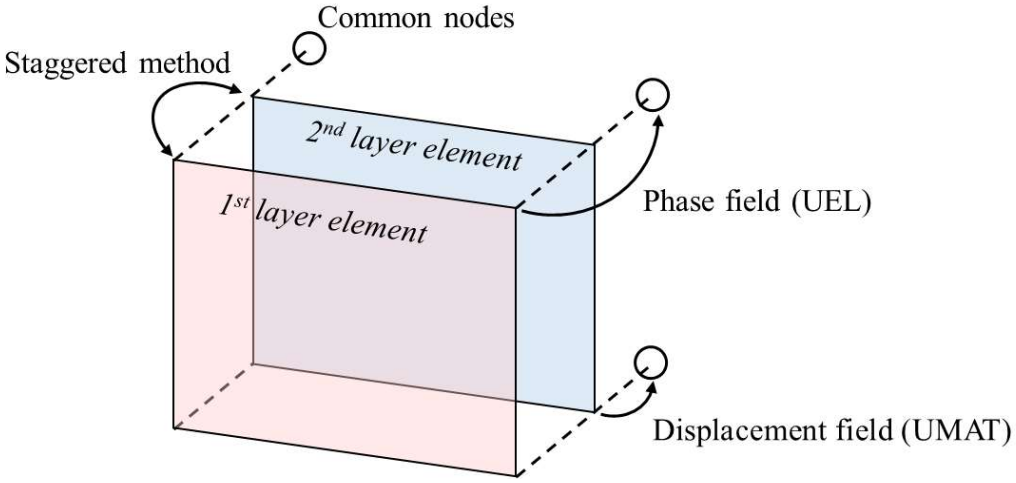

Figure 4, Two-layer finite element structure of the coupled phase field-viscoplasticity method.

4. Finite element models

4.1. Single element model

A single 3D element (i.e. $1\times1\times1$ mm^3 cube) is employed here to simulate the stress-strain response of the material subjected to strain-controlled cyclic load. As shown in Fig. 5, each loading cycle is composed of four steps, i.e., ramp up to the maximum strain, 1 s hold at the maximum strain, ramp down to minimum strain, and 1 s hold at the minimum strain (i.e. 1-1-1-1 trapezoidal waveform). Four strain ranges, i.e. 2.2%, 1.6%, 1.2% and 0.9%, were simulated with a strain ratio of 0.1 and a loading rate of 0.5%/s. The simulations were run for 300 cycles, aiming to capture the cyclic softening behavior.

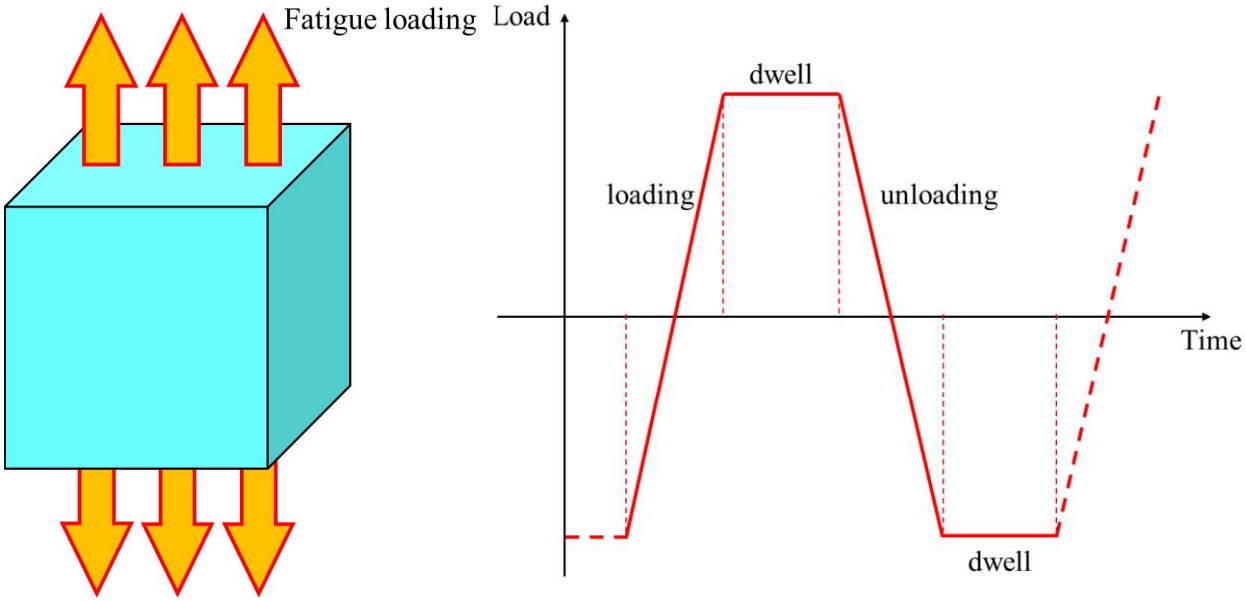

Figure 5, 3D single element model and schematic of the trapezoidal loading waveform.

4.2. 2D CT specimen model

The coupled phase field-viscoplasticity model not only can describe the cyclic deformation but also can capture the crack growth behavior under fatigue conditions. Here, we employed a standard compact tension (CT) specimen to simulate mode I fatigue crack propagation under different loading waveforms. A 2D plane strain finite element model was created for the CT specimen, as shown in Fig.6. Due to the symmetry of CT specimen, only a half model was built, with refined mesh near the crack tip. Cyclic load was applied to a reference node which was tied with the surface of the hole in the model. The initial crack length a was set as 12.2 mm, half the width of the specimen (i.e. a/W=0.5). The cyclic load applied to the specimen was the same as those in experiments (Everitt et al. 2008), with a 1-x-1-1 trapezoidal waveform and a load ratio of 0.1. It should be noted that mesh sensitivity study was carried out by refining the

mesh near the crack tip and along the propagation path. The element size was set as 25, 12.5, 6.25 and 3.125 μm, respectively. The simulation results indicated that the results reached stable at 6.25 μm for both stress and phase fields. Therefore, the model with an element size of 6.25 μm along the crack path was used in our coupled finite element simulations, as shown in Fig. 6.

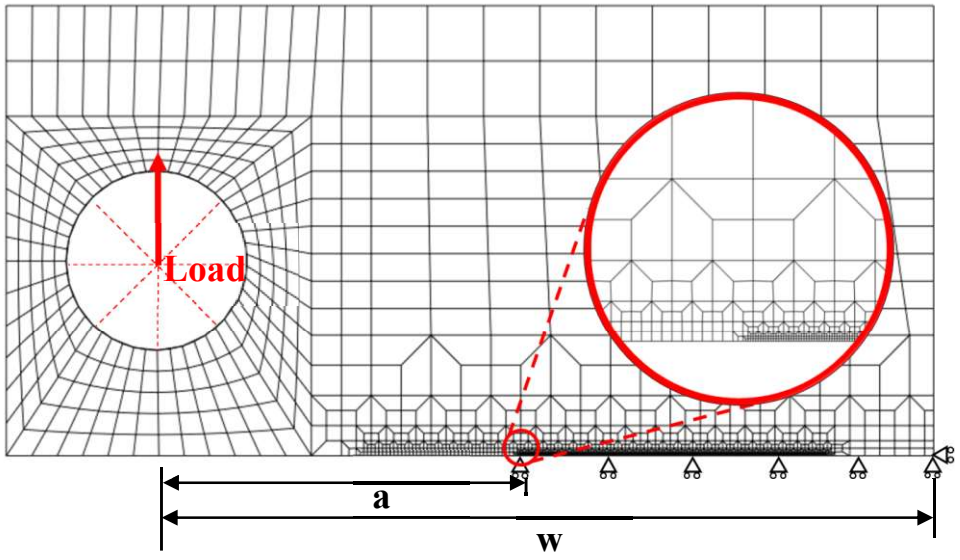

Figure 6, Mesh and boundary condition of the CT specimen model.

4.3. 3D corner crack model

The coupled phase field-viscoplasticity model was also applied to 3D cases, aiming to model the 3D cracks growth. Here, we considered a corner crack specimen, used for crack growth testing in Ref. (Hyde et al. 2010; Tong et al. 2002). The width of the specimen is 5 mm, and the corner crack is quarter circular with a radius of 0.15 mm, as shown in Fig.7(a). Considering the symmetry of the specimen, a half model is generated. A 1-1-1-1 waveform fatigue load is

applied to the specimen, with a maximum load of 50 kN and a load ratio of 0.1. Again, the mesh near the crack tip was refined (element size of ~ 8.19 μm) to improve the convergency of simulations as shown in Fig.7(b).

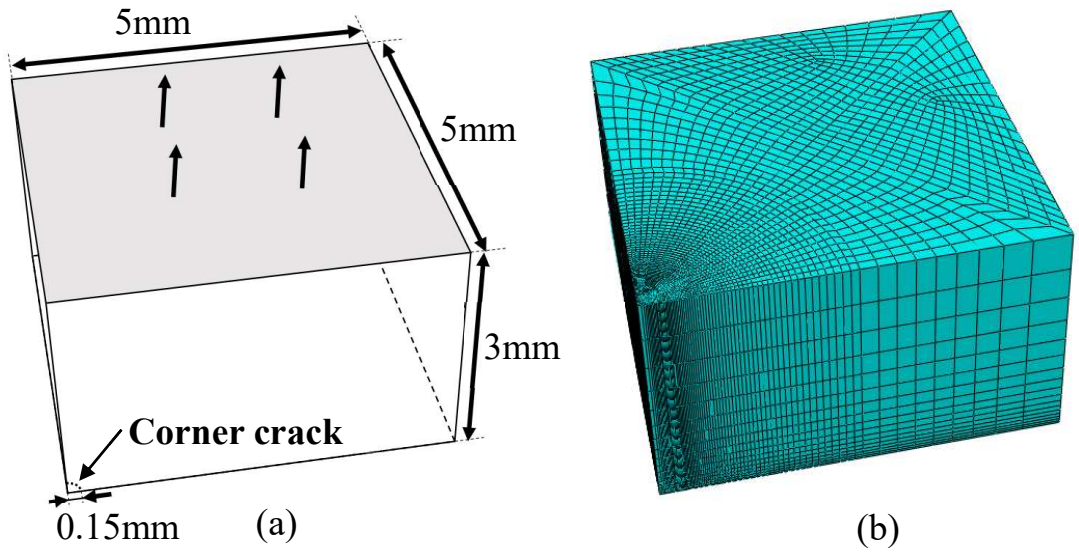

Figure 7, The (a) geometry and (b) mesh of the 3D corner crack model.

4.4. 3D surface crack model

For standard low cycle fatigue tests, most cracks initiate from the surface defects of smooth specimens (Knowles et al. 2002; Daus et al. 2007), leading to crack propagation and final fatigue. Here, we modelled the failure of a cylindrical specimen, with a pre-existing circular defect on the surface, as shown in Fig. 8. The radius of the surface defect is 0.15 mm. The mesh has been refined along the propagation path of the crack to be developed from the surface defect (element size of 8.19 μm). The load condition was the same as that for the corner crack model, with a 1-1-1-1 loading waveform, a peak load of 50 kN and a load ratio of 0.1.

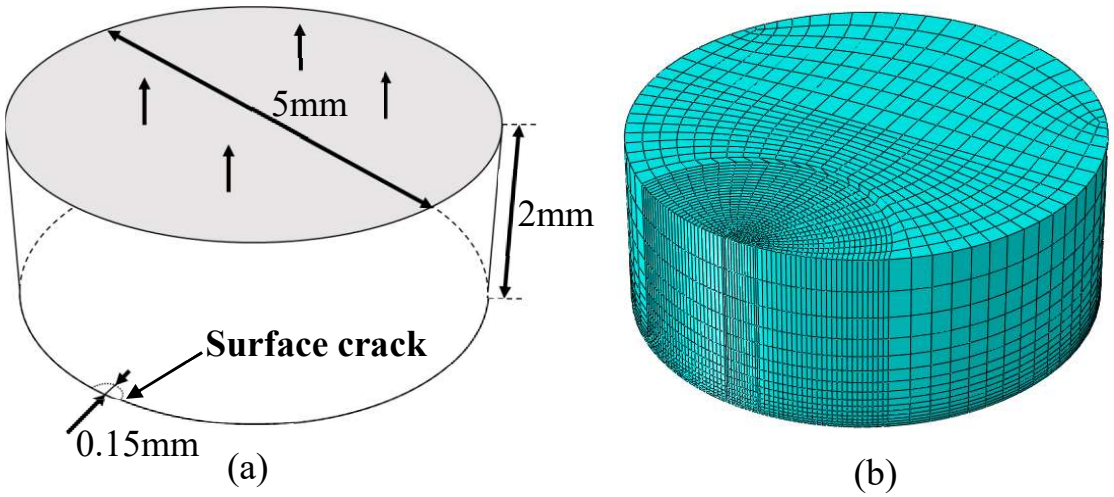

Figure 8, The (a) geometry and (b) mesh of the 3D surface crack model.

4.5. Material and model parameters

In this study, we employed nickel-based superalloy, alloy RR1000, produced via power metallurgy route, in the coupled phase field-viscoplastic model. The corresponding parameter values for the viscoplastic model is given in Table 1 (Zhao et al. 2001), which were calibrated from low cycle fatigue test data of the alloy but without considering softening effect. For alloy RR1000, the fracture toughness and elastic modulus are around 100 MPa·m$^{1/2}$ and 190 GPa, respectively (Zhao et al. 2001 and 2008). The fracture energy density g_f used for phase field simulation was estimated from the fracture toughness and elastic modulus using $g_f=K_{Ic}^2/E$ (Sun et al. 2012), which gave a value of about 50 N/mm. While for crack propagation simulation, considering the cost of calculation, the fracture energy density g_f is chosen as 20 N/mm in order to model the full fracture process within a reasonable amount of time frame. Therefore, we only compare the simulation and experimental results qualitatively based on normalization.

Table 1, Parameters values of the Chaboche model for alloy RR1000 (Zhao et al. 2001).

Parameters	Values
E (MPa)	190000
υ	0.285
b	7.13
Q (MPa)	161.52
a_1 (MPa)	361.57
C_1	391.61
a_2 (MPa)	266.84
C_2	2578.69
Z	678.317
n	15.496
k (MPa)	144.26

5. Results and discussions

5.1 Cyclic softening

Simulation results for the 3D single element model are plotted in Fig. 9, where the hollow symbols represent experimental results from previous study (Zhao et al. 2001). The results indicate that the RR1000 shows a significant cyclic softening after an initial short period of hardening under high strain range. For $\Delta\varepsilon$ = 2.2%, the stress range increases from 1090 MPa to 1156 MPa in 62 cycles, and then decreases to 1093 MPa in 125 cycles. While for specimens with $\Delta\varepsilon$=0.9%, the hardening and softening behavior is not very obvious, in which the stress range increases only from 789 MPa to 791 MPa in 100 cycles, then reduces slowly to 790 MPa after 300 cycles. Similar behavior was also reported in (Abdul-Latif, 1996).

Comparing with experimental data, the coupled phase field-viscoplasticity model shows a good match for both hardening and softening of RR1000, as shown in Fig.9. For strain range of 2.2%, the material experiences a significant hardening process initially, followed by cyclic softening. For strain range1.6%, the stress range increased by about 20 MPa during hardening, and then reduced by 78 MPa after 300 cycles due to softening. While for a strain range of 1.2%, the stress range increased by 11 MPa during hardening and reduced by 38 MPa during softening. The stress range is relative stable for $\Delta\varepsilon$ = 0.9%, changing from 786 MPa to 792 MPa in the initial 100 cycles, and then reducing to 790 MPa after 300 cycles.

Both the experimental and simulation results indicated that the strain range has a great influence on the cyclic hardening and softening behaviors of alloy RR1000, the larger strain range, the more significant the hardening and softening behaviors. During the simulation, the softening and hardening behaviors are mainly controlled by the competition between the internal hardening variables and phase field variable. As described in Eqs. (6) and (11), both hardening and phase variables are function of accumulated plastic strain p. In the first few cycles, the accumulated plastic strain is relatively small, which has little influence on the phase field but increases the hardening variable*s*. However, after a number of cycles, the hardening variable reaches a saturation stage and stabilizes (Chaboche, 1989), thus the phase field variable d, representing the damage in material, starts to take effect, leading to cycle softening.

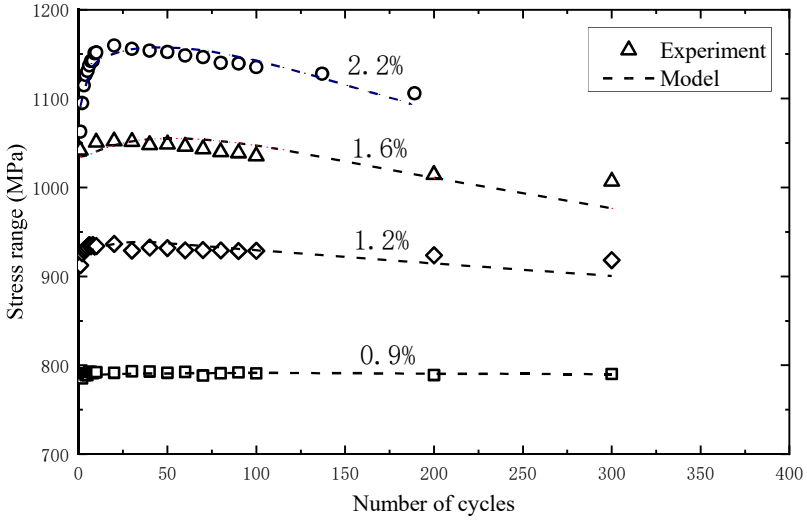

Figure 9, Evolution of stress range with the number of cycles.

In addition, the simulated cyclic loops are demonstrated in Fig.10, in comparison with experimental results. Here, we plotted the stress-strain loops for the first, middle-life and last cycles. The coupled phase field-viscoplasticisty model could describe the cyclic deformation, as well as both hardening and softening behaviors, of the alloy. Good agreement between the simulation and experimental results is obtained. As shown in Fig. 10, in the loading step, the stress increases linearly and then enters the plastic state at about 900 MPa. In the dwell step, the strain stays constant and the stress decreases slightly due to the influence of stress relaxation. Towards the end of unloading step, the material underwent compression to overcome the plastic deformation developed in the loading stage. The compressive stress also decreased in the compressing dwell step caused by the stress relaxation.

The shape and size of strain-stress loops are also affected by the strain range applied to the alloy. For 2.2% strain range, the area of the strain-stress loop in each cycle is larger than others, indicating the accumulation of more plastic energy in each cycle. Therefore, the cyclic hardening and softening are more obvious. For lower strain ranges such as 1.6%, 1.2% and 0.9%, the stress-strain loop becomes thinner, indicating lower plastic energy accumulated in each cycle. Thus, the hardening and softening are less obvious, as shown in Fig. 10.

The strain range also has an influence on the development of phase field variable. As shown in Fig.11, after 189 cycles, the phase field value reaches 0.028 for $\Delta\varepsilon$=2.2%; while for $\Delta\varepsilon$=0.9%, the value is only 0.00379 after 300 cycles. As discussed above, the higher strain range means the development of more plastic deformation in each cycle, resulting in a faster increase of the accumulated plastic strain energy. Therefore, the phase field variable increases quickly when the material is subjected to an increased level of strain range. The rapid growth of phase field variable indicates more damage in each cycle, resulting in more significant softening behavior.

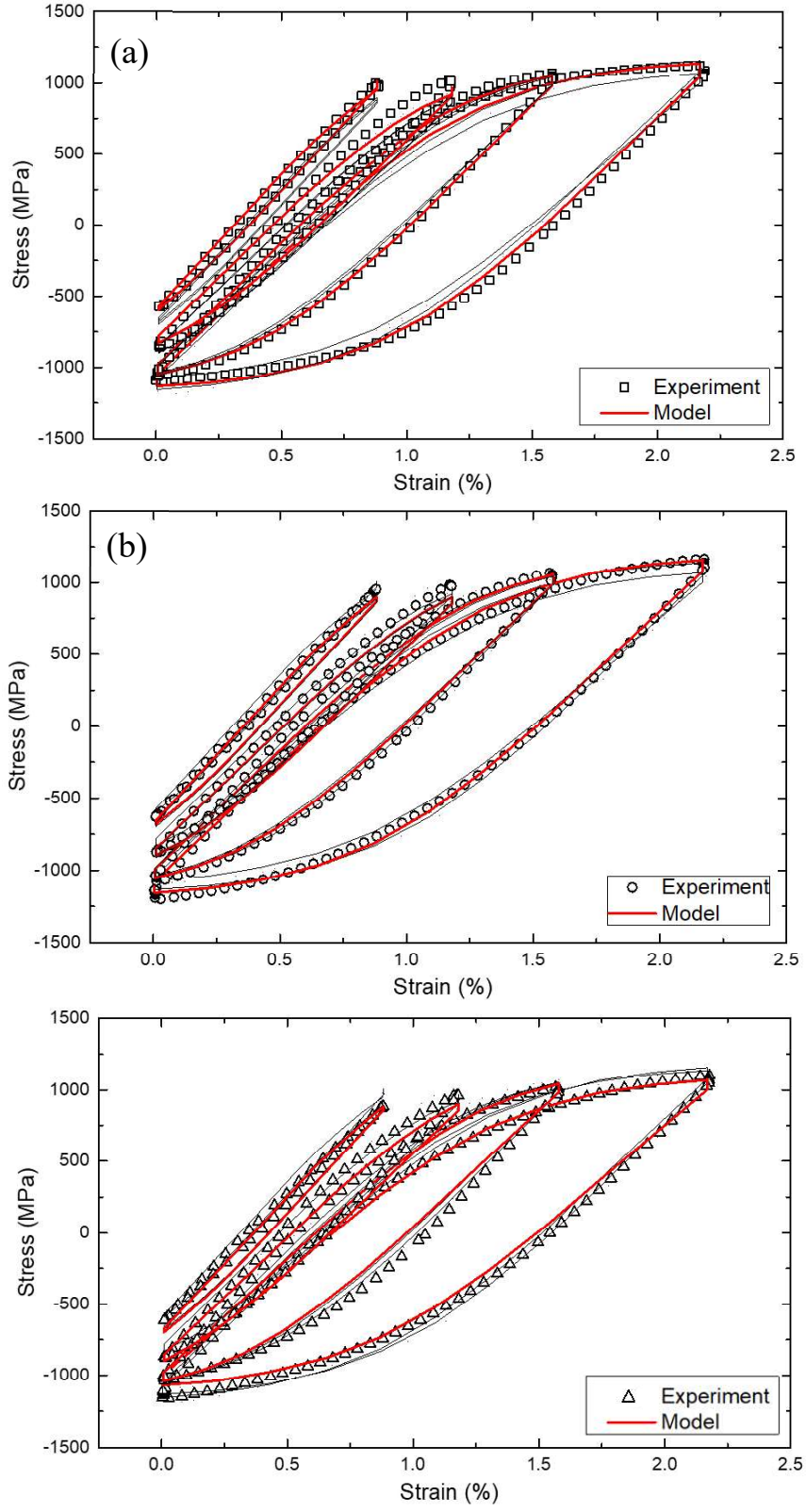

Figure 10, The (a) first, (b) middle-life and (c) final cyclic loops for varied strain ranges: comparison of experimental and simulation results.

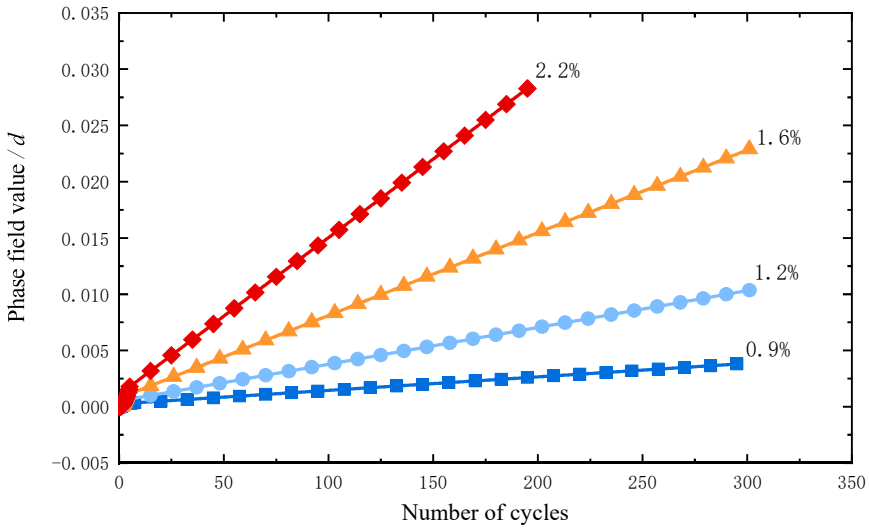

Figure 11, Evolution of phase field value with the number of cycles.

It is worth mentioning that the original viscoplasticity model can also be modified to describe the cyclic hardening and softening behaviors of materials by introducing additional mathematical equations and model parameters (Bernhart et al. 1999; Yaguchi et al. 2005; Takahashi 1998). However, the coupled phase field-viscoplasticity model proposed in this study can handle this situation easily, and only uses the parameter of fracture energy. Moreover, the model can also capture the processes of crack initiation and propagation, which cannot be simulated by the modified viscoplasticity method.

5.2 Model I fatigue crack propagation

The evolution of phase field is shown in Fig.12 for the CT specimen under a 1-1-1-1 loading

waveform. The area with a blue color represents the undamaged material, where the phase field variable is zero. While the area in red represents the extend of facture, indicating the propagation of the crack in the sample. As shown in Fig. 12(a), at the beginning of the simulation, the specimen is a homogeneous solid without damage, for which the phase field equals to zero. After 239 loading cycles, the phase field at the crack tip reached 1, indicating the onset of crack propagation, as plotted in Fig. 12(b). The results indicate that the coupled phase field-viscoplasticity model can capture the crack propagation in standard CT specimens. As described in Eq. (16), the damage and failure of elements are related to the plastic strain accumulated over the fatigue process. When the phase field variable increases to one, the material lose their load-bearing capacity (i.e. degradation of stiffness matrix) and the crack started to propagate.

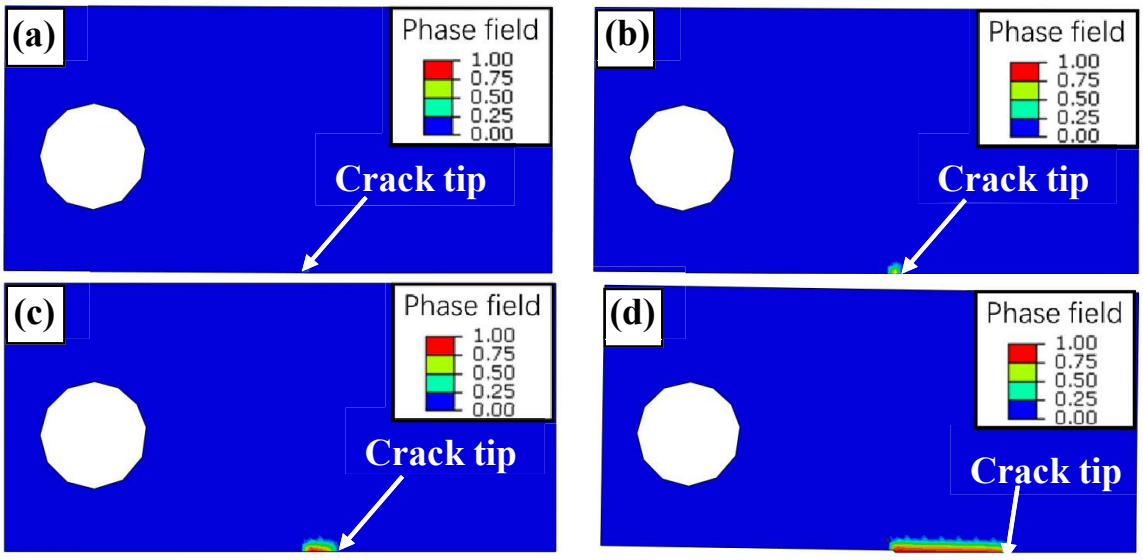

Figure 12, Crack propagation in CT specimens with 1-1-1-1 load waveform at (a) 0, (b) 239, (c) 320 and (d) 476 cycles.

To study the dwell effect, the hold time at the peak load was increased to 20s and 3600s respectively. Fig.13 compares the crack growth rate *da/dN* against ΔK for the 1-1-1-1, 1-20-1-1 and 1-3600-1-1 trapezoidal waveforms. The test data was taken from the work of Everitt et al. (2008) where crack growth tests were carried out for the same CT specimens under the same loading conditions. It is worth mentioning that the *da/dN* data were normalized with respect to the maximum value for both simulation and experimental results. In addition, because the model in this study did not consider the effect of oxidation on the damage or failure of materials, here we used the experimental results obtained in a vacuum condition (Everitt et al. 2008).

As shown in Fig. 13, the modelling results agreed well with the experimental results (Everitt et al. 2008), confirming the capability of the coupled phase field-viscoplasticity model. Both the modelling and test results show that the specimen under 1-20-1-1 waveform has a higher crack growth rate than that under 1-1-1-1 waveform. When the dwell time increased to 3600s, the crack growth rate becomes only slightly higher, as shown in Fig. 13. The difference in crack growth rate is mainly caused by the creep behavior near the crack tip (Everitt et al. 2008). For specimens with long-dwell waveform, the crack tip would undergo a longer state of creep deformation, leading to the accumulation of more plastic strain and hence earlier onset of fracture (Pang et al. 2016). Thus, the crack growth rate for a long dwell is higher, but only modestly, than that for a shorter dwell period. It is worth mentioning that this conclusion is only valid in the vacuum condition. In the air condition, the long dwell time would increase the

crack growth rate significantly (Everitt et al. 2008; Pang et al. 2016), due to the oxidation-accelerated crack propagation behavior, which need to be considered in the future work.

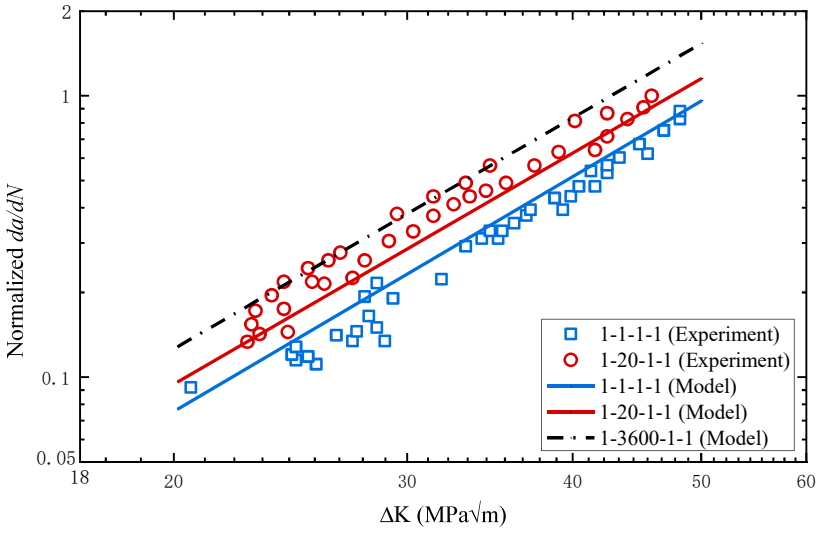

Figure 13, Normalized crack propagation rate as a function of stress intensity factor range for CT specimen with different load waveform; in comparison with experimental data (Everitt et al. 2008).

5.3 Corner crack propagation under fatigue

As shown in Fig.14, the area with a red color represents the failure elements, indicating that the material has been separated by cracks. The simulation results show that the failure of material starts from the front of pre-existed cracks. The crack propagation is perpendicular to the loading direction and the crack length increases with the number of cycles. Because alloy RR1000 is considered as an isotropic material in this study, no crack deflection is observed and

the crack propagation is maintained along the horizontal direction.

During the crack propagation, the shape of crack front changes slightly, from a circular shape to a slightly elliptical shape, termed as “crack tunneling” (Byrne et al. 1993). This is caused by the variation of stress state along the crack front, for which the crack growth rate in the middle of the specimen tends to be higher than that at the surfaces, as shown in Fig.14. Before the crack initiation, the phase field value of the crack front is shown in Fig.15, more or less following the variation of stress intensity factor (Tong 2002). The phase field inside the material is about 1 and reduces to 0.78 on the surface, which means that the inner crack front would accumulate more damage than the surface crack front in each loading cycle.

Generally, for crack front inside the specimen, the stress state is close to a “plane strain” state, while the crack front on the surface is close to a “plane stress” state. As shown in Fig. 15, the stress state factor of the inner crack front is higher than that of the surface crack front, indicating a smaller g_f/η for the inner crack front. According to Eq. (16), the inner crack front would accumulate more damage in each cycle. Therefore, the crack front inside the specimen would grow faster than the crack front on the surface due to the stronger constrain effect which limits the plastic deformation near the crack tip (Forsyth 1978). However, the crack tunneling effect described by the viscoplasic phase field model is not so obvious as the experimental observations (Tong et al. 1997). This is because our simulations are conducted in vacuum condition while the experimental test of corner crack are carried out in air conditions at elevated

temperatures where crack tunneling becomes more significant due to the effect of oxidation.

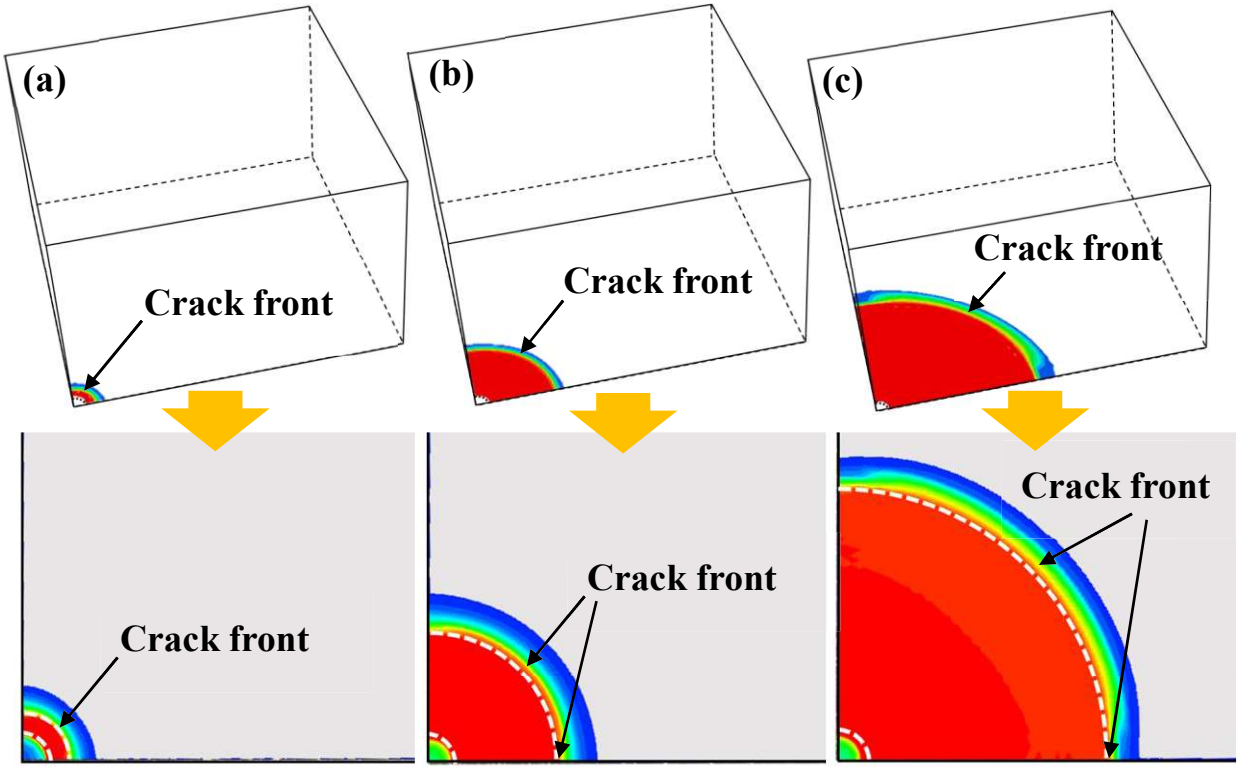

Figure 14, Growth path of 3D corner crack at (a) 5 cycles, (b) 15 cycles and (c) 20 cycles.

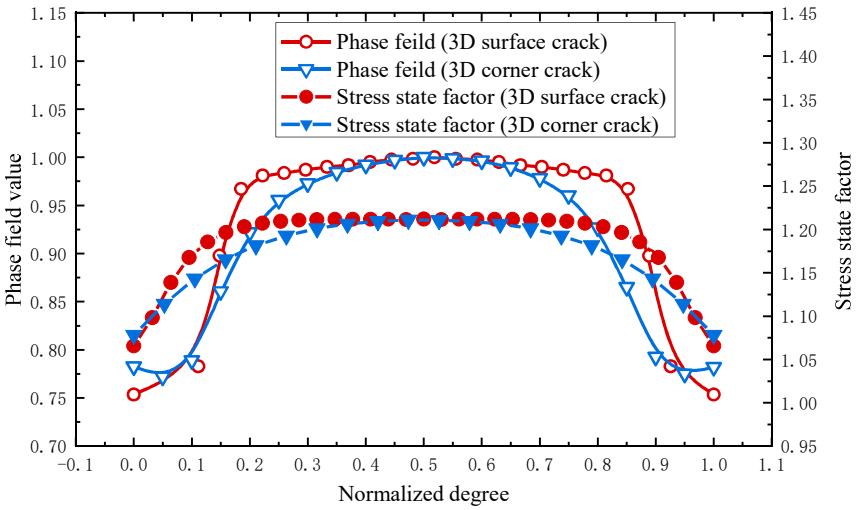

Figure 15, Phase field and stress state factor along the 3D corner and surface crack fronts.

As shown in Fig.16, the computed crack growth rate corresponds with experimental results very well (Pretty et al. 2017), proving the capability of the coupled model in predicting the propagation of 3D corner crack. Here, the crack propagation rate is normalized against the respective maximum values for both simulation and experiment results. Due to the variation of stress state factor, the inner crack front grows slightly faster than that on the surface. Specifically, the crack front in the middle plane gives an upper bound while the crack front on the surface determines a lower bound of the overall crack propagation rate. But the difference between the upper and the lower bounds seems marginal, and comparable to the experimental data (Pretty et al. 2017).

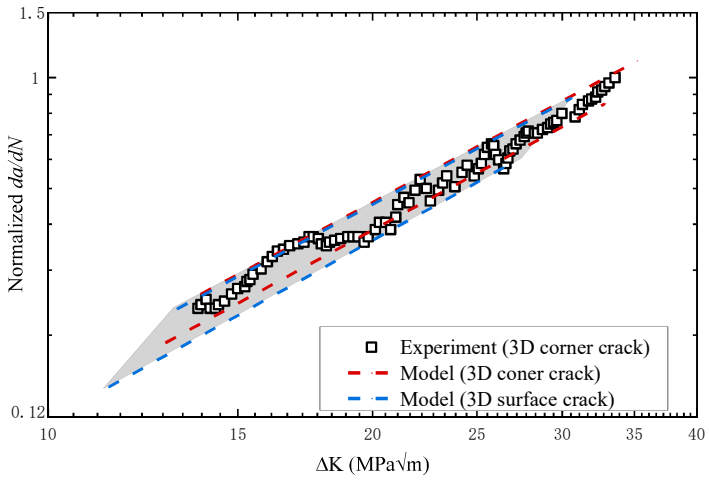

Figure 16, Normalized crack propagation rate as a function of stress intensity factor range for 3D corner and surface cracks; in comparison with experimental data (Pretty et al. 2017).

5.4 Surface crack propagation under fatigue

The surface crack propagation path on a cylinder specimen is shown in Fig. 17, where the crack starts from the pre-existed crack front and propagates through the specimen. Similar to the corner crack case, the surface crack always grows perpendicularly to the loading direction and no crack deflection is observed in the simulation. The evolution of crack front is shown in Fig. 17, where the inner crack front also has a slightly higher growth rate than that on the surface due to the varied stress state along the 3D crack front, as shown in Fig. 15. As the difference is relatively small, the shape of the crack front is more or less semicircular.

As a result of geometry difference, the stress state along the crack front of the 3D surface crack is different from that for the 3D corner crack. As shown in Fig.15, the maximum stress state factor reached 1.2 and occurred at the middle of the crack front. For corner crack, the stress state factor decreased gradually from the middle to the surface crack front. While for surface crack, the stress state factor declined rapidly along the crack front near the surface, indicting a different stress state along the crack front. We also compared the phase field distribution of the 3D surface and corner cracks showing the similar trend to the stress state factor (Fig. 15). The phase field distribution of 3D surface crack indicates that the inner crack front has a more or less uniform growth rate, and the crack front remain almost semicircular during the propagation (Fig. 17). Similar to the 3D corner crack, due to downscaled value of g_f, here we only discuss the trend of crack propagation. As shown in Fig.16, the upper and lower bounds of crack

propagation rate correspond to the crack fronts in the middle plane and on the surface, respectively; very close to those for 3D corner crack as a result of similar constraint (i.e. stress state) along the crack front (Lin et al. 1999; Scott et al. 1981).

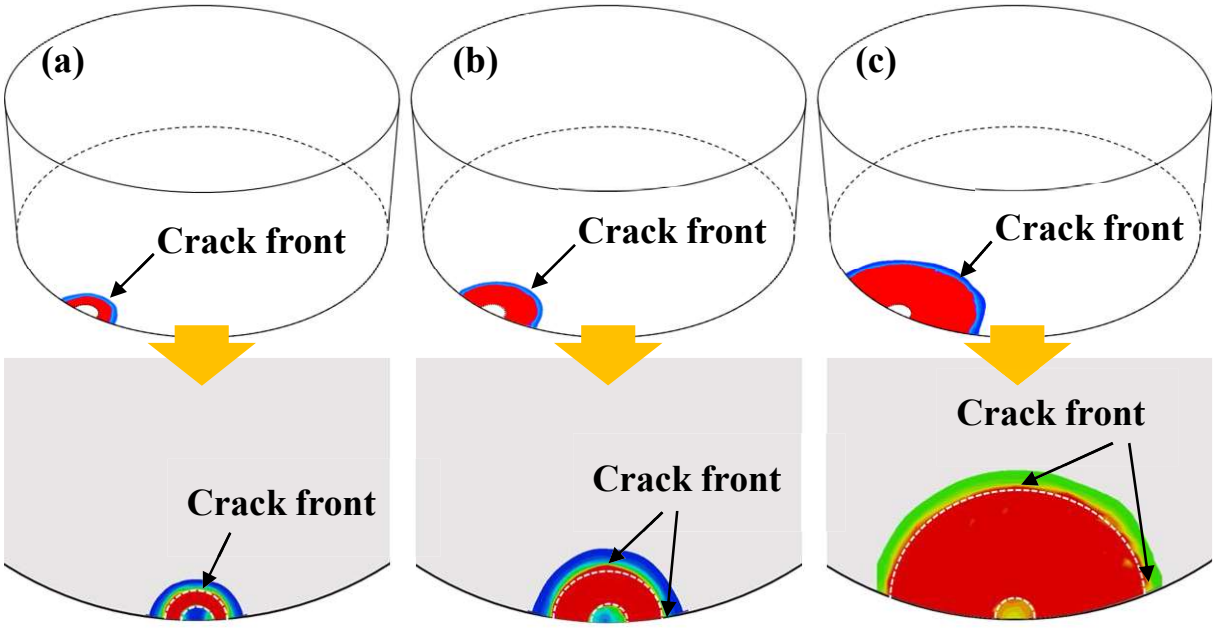

Figure 17, Growth path of 3D surface crack at (a) 10 cycles, (b) 18 cycles and (c) 20 cycles.

The coupled phase field-viscoplaticity model was also employed to study the effect of dwell time on crack propagation of the 3D surface crack under a constant ΔK of 20 and 30 MPa√m. Dwell period in a trapezoidal load waveform was set as 1, 10, 100, 300 and 3600 seconds, respectively. As shown in Fig. 18(a), crack growth rate under ΔK = 30 MPa√m is higher than that under ΔK = 20 MPa√m, due to the increase of load level. Crack growth rate increases with the dwell period, mainly attributed to the creep deformation near the crack front. With the increase of dwell period, accumulated viscoplastic strain near the crack tip in each cycle also

increases, resulting in a faster crack growth rate. In addition, the effect of loading frequency on crack growth rate was also studied for a triangular loading waveform with ΔK = 20 and 30 MPa$\sqrt{m}$, respectively. As shown in Fig. 18(b), crack growth rate becomes higher for increasing stress intensity factor and also increases with the decrease of loading frequency as a result of increased viscoplastic deformation near crack tip for lower loading frequency. Both predictions agree with experimental results (Dalby et al, 2005). It should be noted that environmental effect, especially oxidation at high temperature, was not considered in this study, which would have a significant effect on crack growth rate especially for long dwell period and low loading frequency (Zhao et al. 2008) and needs to be captured in future study.

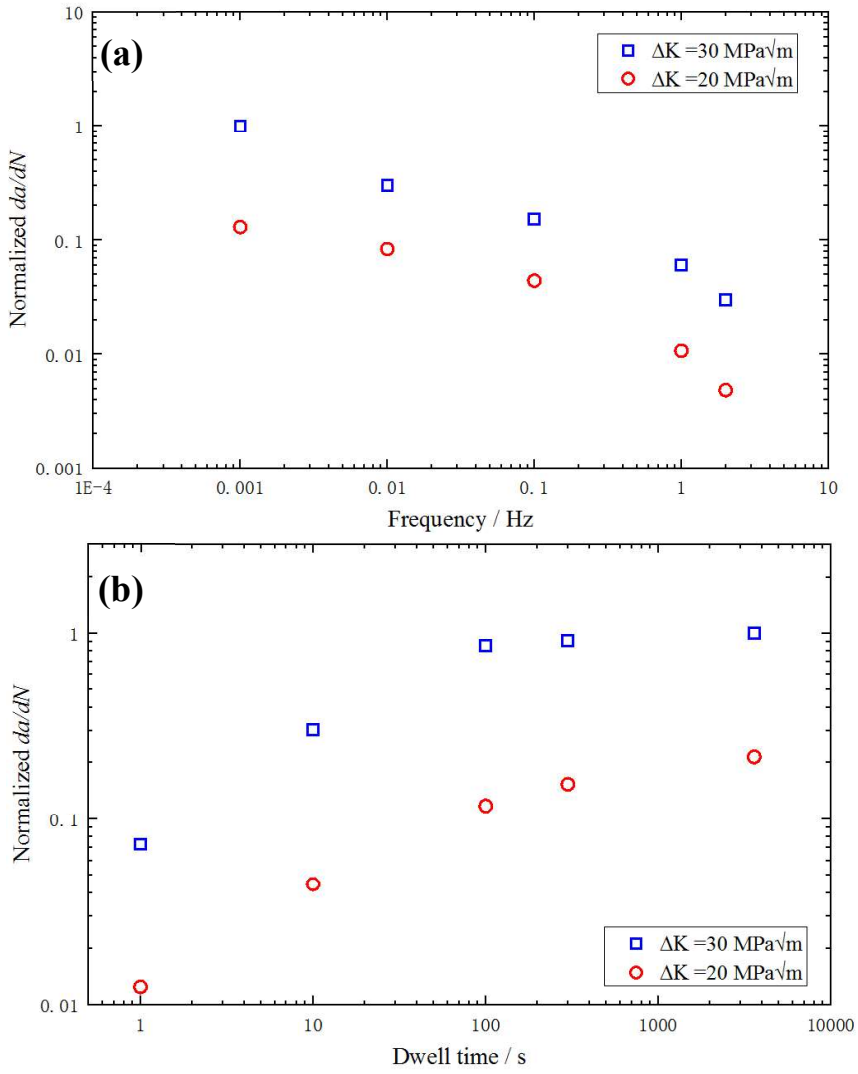

Figure 18, Effects of (a) dwell time (1-x-1-1 waveform) and (b) frequency (simple fatigue waveform) on crack-growth rate for 3D surface crack under constant ΔK.

High-performance alloys (e.g. nickel superalloys studied in this work) are widely used in power generation, nuclear, aerospace, marine and petro-chemical industries. As structural materials, a high resistance to crack initiation and propagation is required to give a required level of damage tolerance design and assessment of the structural components which are often subjected to fatigue and creep in operation. Considerable efforts have been made to understand

the cyclic deformation behaviour of the alloys as well as to develop quantitative models that can predict crack growth in engineering structures/components under operational loading conditions such as helicopter rotation component (Newman et al., 2006) turbine discs (Cláudio et al., 2004) and cold-worked fasteners (Pasta et al., 2007). Many different methods have been developed to predict crack propagation in load-bearing structures and components, such as extended finite element method (XFEM) (Ghandriz et al., 2020), virtual crack closure technique (VCCT) (Karmakov et al., 2020) and cohesive zone method (CZM) (Wang et al., 2020). The phase field approach is a recently developed approach which treats the crack as a smooth transition between the fractured and intact materials, with proved efficiency and robustness (Miehe et al., 2015). In this study, the method has been further extended to model both cyclic deformation (especially cyclic softening) and crack propagation under fatigue and creep loading conditions, which were in good agreement with experimental results. In particular, the phase field method was coupled with a viscoplastic model, for the first time, to model both cyclic deformation and creep-fatigue crack propagation of superalloys at elevated temperature. This has significance in supporting damage tolerance-based design and evaluation of structural components operating under high stress and temperature conditions.

For three dimensional cracks, the crack front is in a multiaxial stress state which is very different from the plane stress or strain states idealised in classical fracture mechanics. The multiaxial stress state also varies along the crack front and imposes a great influence on crack propagation behaviour, as materials can exhibit a transition between ductile and brittle fracture

when the stress state is altered (Smith et al., 2010). However, existing phase field models for three dimensional cracks did not consider the effect of stress state along the crack front, which could cause a discrepancy between simulation and experimental results. In this study, based on the concept of stress triaxiality, a stress state factor η was introduced in the phase field approach to modify the fracture criterion, allowing the effect of multiaxial stress state to be considered in predicting the propagation of three-dimensional cracks. In this approach, critical fracture energy release rate decreases continuously from the surface to the middle of the crack front. Material at the middle of the crack front is subjected to a plane-strain state with a lower critical value, and has a higher crack propagation rate than that on the surface which is subjected to a plane stress state with a higher critical value. The predicted crack growth behaviours agreed well with experimental observations for both corner and surface cracks. This method can be potentially applied to modelling fracture of engineering components subjected to complex and multiaxial loading conditions.

6. Conclusions

In this study, a framework coupling viscoplasticity and phase field was proposed to simulate the deformation and cracking behavior of a nickel superalloy under cyclic loading. The model can capture both cyclic hardening and softening of the material, in good agreement with the experimental results. The simulations indicate that larger strain range induces more damage to the material, leading to more significant cyclic hardening and softening behaviors. Besides, the

model also predicts the crack propagation behavior well, and the results show that the increase of dwell period leads to an increase in crack propagation rate under fatigue. Furthermore, for 3D cracks, the growth rate for the inner crack front is slightly higher than that for the crack front at the surface, due to the varied multiaxial stress state along the 3D crack front. This work is the first attempt to couple the viscoplasticity model with the phase field approach, characterizing the deformation and fracture behaviors of nickel superalloy under fatigue.

7. Acknowledgments

Jianan Song would like to acknowledge the support from the China Scholarship Council (CSC, No. 201906020038) and the Academic Excellence Foundation of BUAA for Ph.D. Students. The work was also funded by the EPSRC (Grant EP/M000966/1 and EP/K026844/1) of the UK and in collaboration with GE Power, Rolls-Royce and dstl.

8. References

Abdul-Latif A. Constitutive equations for cyclic plasticity of Waspaloy. International Journal of Plasticity, 1996, 12(8): 967-985.

Algarni M. Notch Factor Correction Using Stress Triaxiality of Plane-Stress State in High-Cycle Fatigue[J]. International Journal of Fatigue, 2019, 128:105204.

Ambati M, Gerasimov T, De Lorenzis L. A review on phase-field models of brittle fracture and a new fast hybrid formulation. Computational Mechanics, 2015, 55(2): 383-405.

Andersson H, Persson C, Hansson T. Crack growth in IN718 at high temperature. International Journal of Fatigue, 2001, 23(9): 817-827.

B. Bourdin, G.A. Francfort, and J.J. Marigo. The variational approach to fracture. Journal of elasticity, 2008, 91(1):5–148.

B. Schmidt, F. Fraternali, and M. Ortiz. Eigenfracture: an eigendeformation approach to

variational fracture. Multiscale Modeling & Simulation, 2009, 7(3):1237–1266.

Bache MR, Evans WJ, Hardy MC. The effects of environment and loading waveform on fatigue crack growth in Inconel 718. Int J Fatigue 1999;21:S69–77.

Bernhart G, Moulinier G, Brucelle O, Delagnes D. High temperature low cycle behaviour of martensitic forging tool steel. Int J Fatigue 1999;21:179–86

Bhadauria S S, Pathak K K, Hora M S. Determination of critical stress triaxiality along yield locus of isotropic ductile materials under plane strain condition[J]. Materials Science-Poland, 2012, 30(3):197-203.

Byrne J, Hall R, Grabowski L. Elevated temperature crack growth in a nickel base superalloy. In: Ainsworth RA, Skelton RP, editors. Behaviour of defects at high temperatures, ESIS 15. MEP; 1993. p. 367–81.

C. Miehe, L.-M. Schänzel, H. Ulmer, Phase field modeling of fracture in multiphysics problems. Part I. Balance of crack surface and failure criteria for brittle crack propagation in thermo-elastic solids, Comput. Methods Appl. Mech. Eng. 2015, 294 449–485.

C. Miehe, L.-M. Schänzel, Phase field modeling of fracture in rubbery polymers. Part I: finite elasticity coupled with brittle failure, J. Mech. Phys. 2014, Solids 65 93–113.

C. Miehe, M. Hofacker, F. Welschinger, A phase field model for rate-independent crack propagation: robust algorithmic implementation based on operator splits, Comput. Methods Appl. Mech. Eng. 2010, 199 (45–48) 2765–2778.

C. Miehe, M. Hofacker, L.-M. Schänzel, F. Aldakheel, Phase field modeling of fracture in multi-physics problems. Part II. Coupled brittle-to-ductile failure criteria and crack propagation in thermo-elastic-plastic solids, Comput. Methods Appl. Mech. Eng. 2015, 294 486–522.

Castelluccio G M, McDowell D L. Microstructure-sensitive small fatigue crack growth assessment: Effect of strain ratio, multiaxial strain state, and geometric discontinuities. International Journal of Fatigue, 2016, 82: 521-529.

Chaboche J L. Constitutive equations for cyclic plasticity and cyclic viscoplasticity. International journal of plasticity, 1989, 5(3): 247-302.

Chen B, Janssens K G F, Dunne F P E. Role of geometrically necessary dislocation density in multiaxial and non-proportional fatigue crack nucleation. International Journal of Fatigue, 2020, 135: 105517.

Cláudio R A, Branco C M, Gomes E C, et al. Fatigue life prediction and failure analysis of a gas turbine disc using the finite‐element method. Fatigue & Fracture of Engineering Materials & Structures, 2004, 27(9): 849-860.

Dalby S., Tong J., Crack growth in a new nickel-based superalloy at elevated temperature, Part I: effects of loading waveform and frequency on crack growth. J. Mater. Sci. 2005, 40, 1217–1228.

Daus F, Li H Y, Baxter G, et al. Mechanical and microstructural assessments of RR1000 to IN718 inertia welds–effects of welding parameters. Materials Science and Technology, 2007, 23(12): 1424-1432.

Everitt S, Starink M, Reed P. Temperature and dwell dependence of fatigue crack propagation in various heat treated turbine disc alloys. Miner Met Mater Soc, 2008, 10: 741-750.

Fang J, Wu C, Rabczuk T, et al. Phase field fracture in elasto-plastic solids: Abaqus implementation and case studies. Theoretical and Applied Fracture Mechanics, 2019, 103: 102252.

Ferney V. Etude de l'Ecrouissage cyclique sous sollicitations complexes. In: Thèse de Doctorat, Université de Technologie de Compiègne; 1994.

Forsyth PJE. Causes of mixed fatigue-tensile crack growth and significance of micro crack behavior. Met Tech 1978:351–7.

G. A. Haveroth, M. G. Valle, M. L. Bittencourt, et al. A non-isothermal thermodynamically consistent phase field model for damage, fracture and fatigue evolutions in elasto-plastic materials. Computer Methods in Applied Mechanics and Engineering, 2020, 364: 122962.

Ghandriz R, Hart K, Li J. Extended finite element method (XFEM) modeling of fracture in additively manufactured polymers. Additive Manufacturing, 2020, 31: 100945.

Hyde C J, Sun W, Hyde T H, et al. The Effect of a Starter Notch on the Isothermal and Thermomechanical Fatigue Life of a Nickel-Based Superalloy//Pressure Vessels and Piping Conference. 2010, 49255: 347-356.

J. Ulloa, J. Wambacq, R Alessi, et al. Phase-field modeling of fatigue coupled to cyclic plasticity in an energetic formulation. Computer Methods in Applied Mechanics and Engineering, 2020, 373: 113437.

Jahed H, Varvani-Farahani A. Upper and lower fatigue life limits model using energy-based fatigue properties. International journal of fatigue, 2006, 28(5-6): 467-473.

Kanninen M F, Hudak S J, Couque H R, et al. Viscoplastic-dynamic crack propagation: Experimental and analysis research for crack arrest applications in engineering structures. Non-Linear Fracture. Springer, Dordrecht, 1990: 239-260.

Karmakov S, Cepero-Mejías F, Curiel-Sosa J L. Numerical analysis of the delamination in CFRP laminates: VCCT and XFEM assessment. Composites Part C: Open Access, 2020, 2: 100014.

Keck J E, Nicholas T, Palazotto A N. High temperature viscoplastic fatigue behavior of a compact tension specimen. Engineering Fracture Mechanics, 1985, 22(1): 77-91.

Knowles D M, Hunt D W. The influence of microstructure and environment on the crack growth behavior of powder metallurgy nickel superalloy RR1000. Metallurgical and Materials Transactions A, 2002, 33(10): 3165-3172.

Kuhn C, Noll T, Müller R. On phase field modeling of ductile fracture. GAMM - Mitteilungen, 2016, 39(1): 35-54.

Lee C S, Yoo B M, Kim M H, et al. Viscoplastic damage model for austenitic stainless steel and its application to the crack propagation problem at cryogenic temperatures. International Journal of Damage Mechanics, 2013, 22(1): 95-115.

Lin X B, Smith R A. Finite element modelling of fatigue crack growth of surface cracked plates: Part II: Crack shape change. Engineering Fracture Mechanics, 1999, 63(5): 523-540.

M. Hofacker, C. Miehe, A phase field model of dynamic fracture: robust field updates for the analysis of complex crack patterns, Int. J. Numer. Methods Eng. 2013, 93 (3) 276–301.

M.J. Borden, T.J. Hughes, C.M. Landis, A. Anvari, I.J. Lee, A phase-field formulation for fracture in ductile materials: Finite deformation balance law derivation, plastic degradation, and stress triaxiality effects, Comput. Methods Appl. Mech. Eng. 2016, 312 130–166.

Moës N, Dolbow J, Belytschko T. A finite element method for crack growth without remeshing. Int J Numer Methods Eng. 1999, 46(1):131–150

Molnár G, Gravouil A. 2D and 3D Abaqus implementation of a robust staggered phase-field solution for modeling brittle fracture. Finite Elements in Analysis and Design, 2017, 130: 27-38.

N. Singh, C. Verhoosel, R. de Borst, E. van Brummelen, A fracture-controlled pathfollowing technique for phase-field modeling of brittle fracture, Finite Elem. Anal. Des. 2016, 113 14–29.

Newman Jr J C, Irving P E, Lin J, et al. Crack growth predictions in a complex helicopter component under spectrum loading. Fatigue & fracture of engineering materials & structures, 2006, 29(11): 949-958.

Ortiz M, Pandolfi A. Finite-deformation irreversible cohesive elements for three-dimensional crack-propagation analysis. Int J Numer Methods Eng. 1999, 44:1267–1282

Pang H T, Hardy M C, Hide N, et al. Comparison of fatigue crack propagation in nickel base superalloys RR1000 and Udimet 720Li. Materials Science and Technology, 2016, 32(1): 22-39.

Pasta S. Fatigue crack propagation from a cold-worked hole. Engineering Fracture Mechanics, 2007, 74(9): 1525-1538.

Pretty C J, Whitaker M T, Williams S J. Thermo-mechanical fatigue crack growth of RR1000. Materials, 2017, 10(1): 34.

Qian Z, Takezono S, Tao K. Effect of loading frequency on fatigue crack growth under high temperature. International journal of solids and structures, 1996, 33(24): 3601-3610.

Sajid H U, Kiran R. Post-fire mechanical behavior of ASTM A572 steels subjected to high stress triaxialities. Engineering Structures, 2019, 191: 323-342.

Schmidt R, Paris P. Threshold for fatigue crack propagation and the effects of load ratio and frequency. Progress in flaw growth and fracture toughness testing. ASTM special technical publications, 1973, 536: 79-94.

Scott PM, Thorpe TW. A critical review of crack tip stress intensity factors for semi-elliptical cracks. Fatigue Fract Engng Mater Struct, 1981;4:291-309.

Shi X Q, Pang H L J, Zhou W, et al. A modified energy-based low cycle fatigue model for eutectic solder alloy. Scripta Materialia, 1999, 41(3): 289-296.

Smith D J, Ayatollahi M R, Pavier M J. The role of T-stress in brittle fracture for linear elastic materials under mixed-mode loading. Fatigue & Fracture of Engineering Materials & Structures, 2010, 24(2) 137-150.

Su Y, Fu G, Liu C et al. Thermo-elasto-plastic phase-field modelling of mechanical behaviours of sintered nano-silver with randomly distributed micro-pores. Computer Methods in Applied Mechanics and Engineering 2020, 378: 113729.

Sun C T, Jin Z H. Fracture mechanics. Academic Press, 2012.

T.T. Nguyen, J. R´ethor´e, and M.C. Baietto. Phase field modelling of anisotropic crack propagation. European Journal of Mechanics-A/Solids, 2017, 65: 279-288.

T.T. Nguyen, J. R´ethor´e, J. Yvonnet, and M.C. Baietto. Multi-phase-field modeling of anisotropic crack propagation for polycrystalline materials. Computational Mechanics, 2017, 60(2): 289-314.

Takahashi Y. Evaluation of creep-fatigue life prediction methods for low-carbon nitrogen-added 316 stainless steel, Journal of Engineering Materials and Technology-transactions of The Asme, 1998, 120(2): 119-125.

Tong J, Byrne J, Hall R, et al. A comparison of corner notched and compact tension specimens for high temperature fatigue testing. ROLLS ROYCE PLC-REPORT-PNR, 1997.

Tong J, Zhao LG, Lin B. Ratchetting strain as a driving force for fatigue crack growth. Int J Fatigue 2013, 46: 49–57.

Tong J. T-stress and its implications for crack growth. Engineering Fracture Mechanics, 2002, 69(12): 1325-1337.

Wang D, Dong Y, Sun D, et al. A three-dimensional numerical study of hydraulic fracturing with degradable diverting materials via CZM-based FEM. Engineering Fracture Mechanics, 2020, 237: 107251.

Wang J, Guo W, Guo J, et al. The effects of stress triaxiality, temperature and strain rate on the fracture characteristics of a nickel-base superalloy. Journal of Materials Engineering and Performance, 2016, 25(5): 2043-2052.

Yaguchi M, Takahashi Y. Ratchetting of viscoplastic material with cyclic softening, part II: application of constitutive models. Int J Plast 2005;21:835–60.

Ye W M, Hu X T, Guo W L, et al. Three Dimensional Criterion for Creep Crack Propagation in C (T) Specimen. Applied Mechanics and Materials. Trans Tech Publications Ltd, 2017, 853: 142-147.

Zhan Z L, Tong J. A study of cyclic plasticity and viscoplasticity in a new nickel-based superalloy using unified constitutive equations. Part II: Simulation of cyclic stress relaxation. Mechanics of Materials, 2007, 39(1): 73-80.

Zhang S, Jiang W, Tonks M R. A new phase field fracture model for brittle materials that accounts for elastic anisotropy. Computer Methods in Applied Mechanics and Engineering, 2020, 358: 112643.

Zhao L G, Tong J, Vermeulen B, et al. On the uniaxial mechanical behaviour of an advanced nickel base superalloy at high temperature. Mechanics of materials, 2001, 33(10): 593-600.

Zhao L G, Tong J. A viscoplastic study of crack-tip deformation and crack growth in a nickel-based superalloy at elevated temperature. Journal of the Mechanics and Physics of Solids,

2008, 56(12): 3363-3378.